Materials Today Physics 27 (2022) 100755

Contents lists available at ScienceDirect

Materials Today Physics

journal homepage: www.journals.elsevier.com/materials-today-physics

Tension-induced phase transformation and anomalous Poisson effect in violet phosphorene

Penghua. Ying [a], Xiaowen. Li [b], Xiaobin Qiang [b], Yao Du [a], Jin Zhang [a,**], Lang Chen [b,***], Zheng Zhong [a,*]

[a] School of Science, Harbin Institute of Technology, Shenzhen, 518055, PR China
[b] Department of Physics, Southern University of Science and Technology, Shenzhen, 518055, PR China

ARTICLE INFO

Keywords:
Violet phosphorene
Poisson's ratio
Phase transformation
Strain engineering
Mechanical anisotropy

ABSTRACT

Two-dimensional violet phosphorene (VP) nanosheets are promising semiconductor materials with unique cross structures distinct from those of their allotropes such as black phosphorene and blue phosphorene, but their mechanical behaviors remain almost unexplored. By using the first-principles calculations, in this paper we investigate the mechanical behaviors of monolayer, bilayer, and bulk VP under uniaxial tension. A phase transformation from the open-pore phase to closed-pore phase is observed in VP structures when under a specific tensile strain. It is revealed that the phase transformation is attributed to the competition between the rotation and elongation of sub-nano rods in VP structures during the loading process. Due to the phase transformation, the in-plane Poisson's ratio of monolayer VP can become greater than 1.2, while the bulk VP possesses a negative out-of-plane Poisson's ratio with a magnitude up to -0.3 at a certain strain. These results indicate that Poisson effects in VP are superior to those in any other existing two-dimensional materials. In addition, based on the tensor analysis of elastic constants, a strong mechanical anisotropy is observed in VP structures both before and after the phase transformation. Besides the mechanical properties, the band gap of all VP structures decreases as the applied tensile strain increases, which can eventually transform into the metallic state prior to their fracture. The combination of unique phase transformation, anomalous Poisson effect, strong mechanical anisotropy and tunable electronic properties render VP be a novel nanoscale metamaterial with multifunctional applications.

1. Introduction

Two-dimensional (2D) materials such as graphene and black phosphorene (BP) are attracting a great deal of attention due to their unique physical properties and the corresponding novel phenomena [1,2]. Different to the zero band gap of semimetal graphene, BP is a semiconductor with the direct band gap ranging from 0.3 eV (bulk) to 2.0 eV (monolayer) [3]. Specifically, the high carrier mobility together with the high optical and ultraviolet absorption of BP makes it appealing for the use in next-generation optoelectronics [2]. However, the chemical instability such as fast oxidation and degradation of BP has been recognized as the bottleneck in its applications. Very recently, another allotrope of layered phosphorus named violet phosphorus (VP) was synthesized in experiments [4], which was demonstrated to be a semiconductor with a direct band gap of 1.7 eV [4]. Moreover, the VP having a unique 2D nanosized cross structure [5] was proven to be more thermally and chemically stable than its BP counterpart [4,6], though BP was previously considered as the most stable phosphorus allotrope. In other words, VP possesses a much better thermal and chemical stability performance than its BP and, simultaneously, can retain the direct band gap property, which suggest that VP materials are more promising candidates for semiconductor-related applications [7].

Understanding the mechanical properties of 2D semiconducting materials is not only crucial for the reliability of their applications in practical working environment but also of fundamental importance for the coupling between mechanical and other physical properties [8]. For example, the strain engineering technique has been extensively employed in previous studies to tune the electronic, optical, thermal, and piezo/flexoelectrical properties of 2D semiconducting materials [9]. Unlike its BP counterpart whose mechanical properties have been

* Corresponding author.
** Corresponding author.
*** Corresponding author.
E-mail addresses: jinzhang@hit.edu.cn (J. Zhang), chenlang@sustech.edu.cn (L. Chen), zhongzheng@hit.edu.cn (Z. Zhong).

https://doi.org/10.1016/j.mtphys.2022.100755
Received 21 March 2022; Received in revised form 14 May 2022; Accepted 9 June 2022
Available online 22 June 2022

extensively investigated theoretically and experimentally [10–12], the investigation on mechanical properties of VP is currently very limited. Until very recently, the initial experimental attempt [5] was conducted with the aid of atomic force microscope (AFM) based nanoindentation. The VP was demonstrated to possess an extremely high deformation resistance. The 2D Young's modulus of monolayer VP was reported to be 1512 ± 76 N m^{-1}, which is 4.4 times as high as that of graphene. However, restricted by the loading method of the AFM-based nanoindentation, the mechanical behavior of VP under in-plane uniaxial tension cannot be fully revealed in the existing experiments. Furthermore, owing to its unique cross structure at the nanoscale, it is expected that the VP may have a distinct mechanical behavior under in-plane loading, which may have a strong influence on its band gap property, similar to the strain engineering of band gaps of other 2D materials such as graphene [13], hexagonal BN [14], MoS_2 [15], and Bi_2O_2Se [16].

To this end, in the present work the first-principles calculations are performed to investigate the mechanical behaviors of monolayer, bilayer, and bulk VP under uniaxial tension. A tension-induced phase transformation phenomenon is observed in all VP structures. The thermodynamic and mechanical stability of the new phase is verified by molecular dynamics simulations and Born stability criteria. The mechanical properties of transformed new phase are compared with the values of its parent counterpart. Moreover, during the tension process of VP structures, an extremely large Poisson's ratio is found in the in-plane direction while a negative Poisson's ratio is found in the out-of-plane direction. This anomalous Poisson effect is explained by analysing the deformation mechanism of VP structures. In addition, the band gap of all VP structures is found to decrease with growing tensile strain, which eventually can transform into the metallic state at a large tensile strain. Our work not only reveals the potential of VP as nanoscale metamaterial with an extremely large in-plane Poisson's ratio and a negative out-of-plane Poisson's ratio from a fundamental perspective but also facilitates the applications of VP as a new class of band gap-tunable semiconductor derived by strain engineering.

2. Models and methods

The initial atomic structures of VP are shown in Fig. 1, the corresponding lattice parameters of which were extracted from the references [4,17]. The VP materials with different thickness, i.e., monolayer, bilayer, and bulk VP structures were considered in this work to investigate the effect of thickness on the mechanical behaviours of VP. The VP consisting of two layers has a orthogonal network structure (see Fig. 1 (a)), in which each component layer is composed of cross sub-nano rods with -[P2]-[P8]-[P2]-[P9]- repeating units and connected with the other layer through [P9] unit linking (see Fig. 1(c)). The side view of bulk VP considered in simulations is shown Fig. 1(b), while the simulation models of monolayer and bilayer VP can be further obtained by adding a sufficient vacuum layer of 15 Å in the cross-plane plane (z direction).

First-principles calculations on mechanical properties and energy band structures were performed at the level of density functional theory (DFT), which were implemented through Vienna Ab initio Simulation Package (VASP) [18] with the aid of SCAN *Meta*-GGA + rVV10 vdW functional form [19]. The calculations were converged with an energy tolerance of 10^{-5} eV and a force tolerance of 0.01 eV/Å under a cutoff energy of 500 eV. All computations were carried out by automatic k-mesh generators with $l = 0.03$, where l in the unit of 2π/Å is the k-points resolved value between adjacent k-points in reciprocal cell and. The number N of k-points is further determined from

$$N = \max\left(1, \left|\vec{b}\right| / l\right), \tag{1}$$

where $\vec{b}$ is the reciprocal lattice vector in the specific direction. The optimized lattice parameters of monolayer, bilayer, and bulk VP are 8.89 Å × 9.00 Å, 8.89 Å × 9.03 Å, and 8.92 Å × 9.10 Å × 20.56 Å, respectively, which are comparable to the experimental results [4].

3. Results and discussions

In this section, the mechanical responses, phase transformation, and electronic properties of VP structures obtained from DFT calculations are discussed. Efforts are made to further explain the mechanism of some observed novel phenomenon including anisotropic elastic properties, the extremely large in-plane Poisson's ratio, and the negative out-of-plane Poisson's ratio.

3.1. Tension-induced phase transformation

We first investigated the mechanical behaviours of monolayer, bilayer, and bulk VP under uniaxial tension. Considering the similarity of the atomic structure of VP along x and y directions, the tension was applied only along the x direction, while the stress along the lateral direction (y direction) was released to zero. The unit cells of monolayer, bilayer, and bulk VP, respectively, containing 42, 84, and 84 atoms were employed here to simulate their tensile behaviors. Herein, we define the engineering strain as $\epsilon_i = 1 - L_i/l_i$, where L and l denote the crystal lengths of the structure after and before deformation, respectively, and

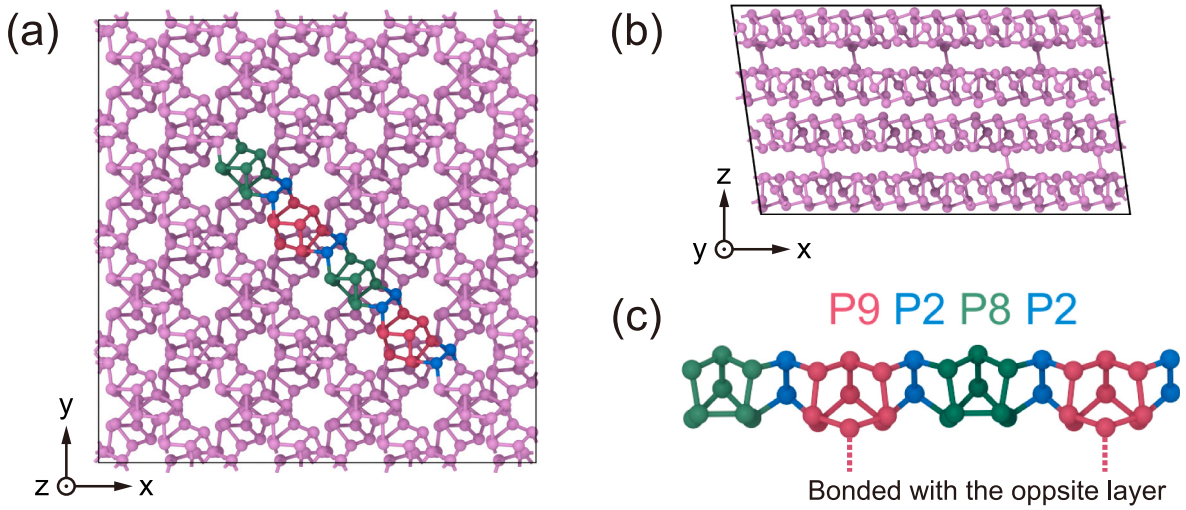

Fig. 1. Atomic structures of VP considered in this work. (a) Top view of monolayer VP. (b) Side view of bulk VP. (c) The sub-nano rods of VP consisting of -[P2]-[P8]-[P2]-[P9]- repeating units. Here, the 4 × 4 × 1 supercells are presented for clarity. All atomic structures are drawn with aid of OVITO package [20].

the subscripts $i = x$, y and z correspond to lengths in the x, y and z directions, respectively. The uniaxial tension was applied with a small strain increment of 1% each step. In this loading process, the corresponding stress was calculated as the total force divided by the cross-sectional area that is L_yL_z. In calculating the stress of VP structures during the tensile process, the thickness L_z of monolayer, bilayer and bulk counterparts under tension was, respectively, defined as L_z^0, $2L_z^0$ and $2L_z^0$, where $L_z^0 = 10.28$ Å equalling to the layer separation in pristine bulk VP without tension [21–24].

The in-plane and out-of-plane Poisson's ratios, i.e., υ_{in} and υ_{out}, can be further obtained:

$$\upsilon_{in} = -\frac{\epsilon_y}{\epsilon_x}, \quad \upsilon_{out} = -\frac{\epsilon_z}{\epsilon_x}. \tag{2}$$

In calculating υ_{out}, the thickness L_z of bulk VP was defined as the cell length in the z direction, while L_z of both monolayer and bilayer VP was similarly defined as the vertical distance of the farthest atomic pairs [21, 23,25].

Fig. 2 shows the evolution of stress (σ_x), strain energy (U), and Poisson's ratios (υ_{in} and υ_{out}) of VP structures with increasing strain (ϵ_x) until fracture. From Fig. 2(a), it can be found that the whole tension process of VP mainly includes three stages. At the first stage, σ_x increases linearly with growing ϵ_x when $0 < \epsilon_x \lesssim 0.05$ and then keeps around a constant value at $0.05 \lessapprox \epsilon_x \lessapprox 0.1$, which corresponds to the transformation from the elastic deformation to the plastic deformation. At the second stage, σ_x keeps decreasing with growing ϵ_x when $0.1 \lessapprox \epsilon_x \lessapprox 0.2$ and finally reaches the minimum value at $\epsilon_x \approx 0.2$, showing an abnormal negative-stiffness behavior at this stage. At the final stage ($\epsilon_x \gtrapprox 0.2$), σ_x turns to increase monotonically with increasing ϵ_x until the final fracture of VP. As for three VP structures with different thicknesses considered here, the fracture strain is found to decrease with increasing thickness, while the tensile strength of different VP structures follows the order of monolayer > bulk > bilayer. Specifically, according to Fig. 2(a), values of the tensile strength of monolayer, bilayer, and bulk VP are 14.15 GPa, 12.30 GPa, and 12.82 GPa, respectively, while the corresponding fracture strains are, respectively, 0.49, 0.45, and 0.42. Herein, the fracture strain is defined as the strain corresponding to the maximum stress, i.e., tensile strength.

For monolayer and bilayer VP structures, their abnormal negative-stiffness behavior at the second stage leads to twice appearances of zero stress under tension (see Fig. 2(a)). These two zero-stress points at the $\sigma_x - \epsilon_x$ curves successively correspond to the maximum and the minimum points in the $U - \epsilon_x$ curves shown in Fig. 2(b). Specifically, the minimum point of U indicates the onset of phase transformation occurring in monolayer and bilayer VP structures due to tensile loading (see the inset in Fig. 2(b)), while the maximum point of U corresponds to the energetic barrier of phase transformation. The new phases of monolayer and bilayer VP structures are metastable, because the energy of new phases is slightly higher than that of the parent phase. Different from monolayer and bilayer VP structures, a discontinuous variation of U with growing ϵ_x is observed in the bulk VP structure, since a sudden drop of U occurs at $\epsilon_x \approx 0.24$. This sudden drop of the energy of bulk VP is also accompanied by a sudden drop of its stress (see Fig. 2(a)). We attribute this energy and stress drop phenomenon to the interlayer slip occurring in the phase transformation process of bulk VP structure, which will be discussed in details in section 3.4.

Fig. 2(c) and (d), respectively, shows the evolution of υ_{in} and υ_{out} with growing ϵ_x. It is found that υ_{in} first increases with growing ϵ_x when

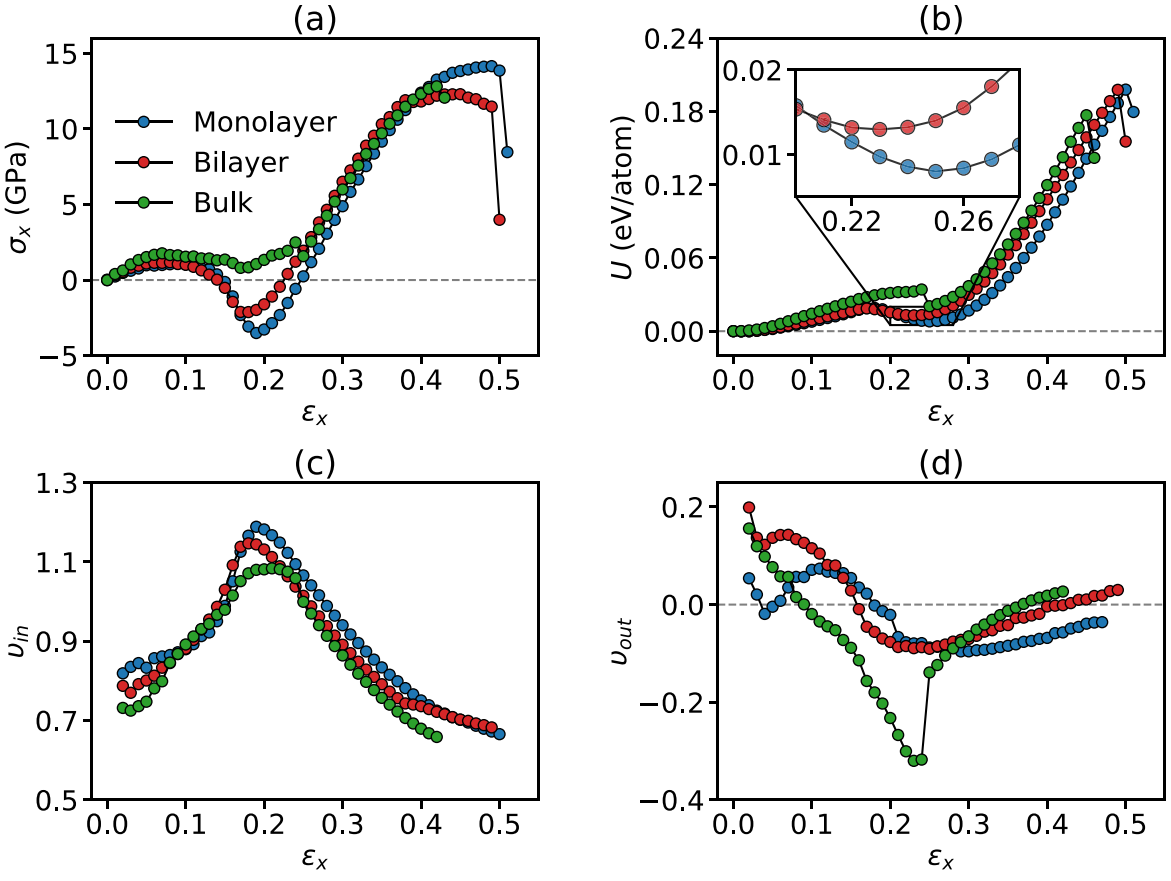

Fig. 2. Evolution of (a) stress σ_x, (b) energy U, (c) in-plane Poisson's ratio υ_{in}, and (d) out-of-plane Poisson's ratio υ_{out} of monolayer, bilayer, and bulk VP during the tensile loading process. Here, the inset in (d) shows the thickness definition of bilayer VP.

$\epsilon_x \lessapprox 0.2$. Afterwards, when $\epsilon_x \gtrapprox 0.2$, υ_{in} begins to decrease as ϵ_x increases. In other words, the change in υ_{in} with varied ϵ_x generally exhibits a convex parabolic shape, which reaches the maximum value at $\epsilon_x \approx 0.2$. Specifically, the maximum values of υ_{in} are 1.20, 1.15, and 1.08 for monolayer, bilayer, and bulk VP structures, respectively. All of these values are larger than one, which indicates that the magnitude of the responded transverse strain ϵ_y is much larger than that of the applied longitudinal strain ϵ_x. As for all VP structures, their υ_{out} is positive at the initial stage. However, when under tensile loading, υ_{out} can shift from the initial positive value to a negative value with the transition occurring at the strains of 0.18, 0.16, and 0.10 for monolayer, bilayer, and bulk VP structures, respectively. The maximum negative υ_{out} of monolayer, bilayer, and bulk VP are -0.096, -0.091, and -0.320, which are observed at $\epsilon_x = 0.29$, 0.25, and 0.23, respectively. Here, the maximum negative υ_{out} refers to the negative υ_{out} with the maximum absolute value.

Taking monolayer VP as an example, we show in Fig. S1 (see supplementary materials) the evolution of stress σ_x and energy U of both $1 \times 1 \times 1$ and $2 \times 2 \times 1$ supercells during the similar tensile simulations to examine the effect of the size of the supercell on the tensile behaviors. In general, results of these two models are qualitatively similar to each other, though a small quantitative difference is observed. This result further proves the existence of unique mechanical behaviors such as the negative stiffness and phase transformation behaviors in VP, irrespective of the supercell size of VP considered in simulations. In Table 1, we compare υ_{out} of VP structures considered in the present work with the values of υ_{out} previously reported for some other monolayer and bilayer 2D materials similarly possessing the out-of-plane auxetic property. When compared with their black counterparts [21], the present VP structures are found to possess a more significant auxetic behavior. In addition, the maximum negative υ_{out} of the present VP structures is comparable to values of other monolayer black phosphorene-like structures [22,26,27], monolayer M_2Se_3 [28], bilayer graphene and graphene-based heterostructures [29,30], but is much smaller than that of monolayer X_3M_2 [23].

Based on $\sigma_x - \epsilon_x$ and $U - \epsilon_x$ curves shown in Fig. 2(a) and (b), the tension-induced phase transformation can be clearly detected in VP structures with different thicknesses. To determine the atomic structures of VP after the phase transformation, the new phases of monolayer, bilayer and bulk VP structures are obtained after performing the geometric optimization to their structures at the tensile strains of 0.24 for monolayer VP, 0.22 for bilayer VP, and 0.25 for bulk VP, respectively, which correspond to critical strains at the onset of their phase transformation as shown in Fig. 2(b). Fig. 3(a) shows atomic structures of the parent and transformed phases of monolayer VP. It can be seen that the transformed phase has an asymmetric structure, which shows a closed-pore structure enclosed by the cross sub-nano rods. This is distinctly different with the open-pore structure of the parent phase of monolayer VP. The similar closed-pore structure is also found in the transformed phases of both bilayer and bulk VP. Thus, the parent phase and transformed phase of VP are named here as op (open-pore) phase and cp (closed-pore) phase, respectively. The lattice constants of op and cp phases are listed in Table 2. To quantitatively compare the structure changes induced by the phase transformation, we further calculate the in-plane angle θ between the cross sub-nano rods of op and cp phases. By assuming that the sub-nano rods before and after phase transformation remain straight, θ can be estimated as:

$$\theta = \arctan\frac{2L_y}{L_x}. \tag{3}$$

We find that θ of op and cp phases approximately equals to 90° and 60° (see Fig. 3(a)), respectively, indicating a structural transformation from the orthogonal network to a skew network for VP structures. In addition to the structure changes observed in the in-plane directions, the thickness (i.e., L_z) of bilayer and bulk VP structures is found to increase from 21.56 Å and 20.56 Å at the parent op phase to 22.09 Å and 21.36 Å at the transformed cp phase, respectively, which is consistent with the out-of-plane auxetic behavior mentioned before (see Fig. 2(d)).

To verify the thermodynamic stability of VP structures after phase transformation, taking the monolayer VP as an example, we preformed *ab initio* molecular dynamics (AIMD) simulations of its cp phase for 5000 steps. In doing this, a $2 \times 2 \times 1$ supercell based on the optimized structure containing 168 atoms was simulated within the NVT ensemble using Andersen thermostat at 300 K, a time step of 2 fs, and a $1 \times 1 \times 1$ *k*-point mesh. The AIMD simulations were totally run for 10 ps. The energy evolution during the entire simulation is plotted in Fig. 3(b). It is found that the energy reaches equilibrium rapidly at the beginning of AIMD simulations and remains almost unchanged afterwards. Moreover, the structure obtained from AIMD simulations at the time of 10 ps (see insects in (Fig. 3(b))) is almost identical to the original cp phase of monolayer VP (Fig. 3(a)) without any bond breakages or disorders. These results indicate the thermodynamic stability of the transformed cp phase of VP structures.

Table 1
Out-of-plane Poisson's ratios of VP structures and other 2D crystals reported before.

Classification	Material	Value
	Black phosphorene [21]	−0.027
Monolayer black phosphorene	*α*-arsenene [26]	−0.093
Monolayer black phosphorene	MX [22]	−0.004, −0.210, −0.208, −0.433
	BP_5 [27]	−0.037
Monolayer M_2Se_3	Co_2Se_3 [28]	−0.24
	Ni_2Se_3 [28]	−0.22
	Pd_2Se_3 [28]	−0.20
Monolayer X_3M_2	S_3N_2 [23]	−0.754
	Se_3N_2 [23]	−0.288
	S_3P_2 [23]	−0.706
	Se_3P_2 [23]	−0.679
	S_3As_2 [23]	−1.292
	Se_3As_2 [23]	−0.556
Bilayer graphene and Graphene-based heterostructures	Bilayer graphene [29]	−0.061
	Graphene/MoS_2 [29]	−0.090
	Graphene/h-BN [30]	−0.111
VP structures	Monolayer VP	−0.096
	Monolayer VP	−0.091
	Bulk VP	−0.320

3.2. Anisotropic elastic properties

In section 3.1, we revealed the tension-induced op-to-cp phase transformation in VP structures and further demonstrated the thermodynamic stability of the transformed cp phase at the finite temperature. In this section, we further investigate the elastic properties of cp phases and compare the mechanical properties of the transformed phase to those of its parent counterpart.

Since monolayer and multi-layer VP structures in current work can be considered as 2D rectangular system, we only consider the 2D elastic constants of VP under the in-plane stress condition using Viogt scheme [31]. Under this circumstance, the constitutive equation of VP can be written as:

$$\begin{bmatrix}\sigma_1\\ \sigma_2\\ \sigma_6\end{bmatrix} = \begin{bmatrix}C_{11} & C_{12} & 0\\ C_{12} & C_{22} & 0\\ 0 & 0 & C_{66}\end{bmatrix}\begin{bmatrix}\epsilon_1\\ \epsilon_2\\ \epsilon_6\end{bmatrix}, \tag{4}$$

where σ_i and ϵ_j indicate the stress and strain, C_{ij} is the elastic constant tensor, $i, j = 1$, 2, and 6 in the Voigt notation correspond to *xx*, *yy*, and *xy* in tensor notation, respectively. Based on the elastic constants, one can

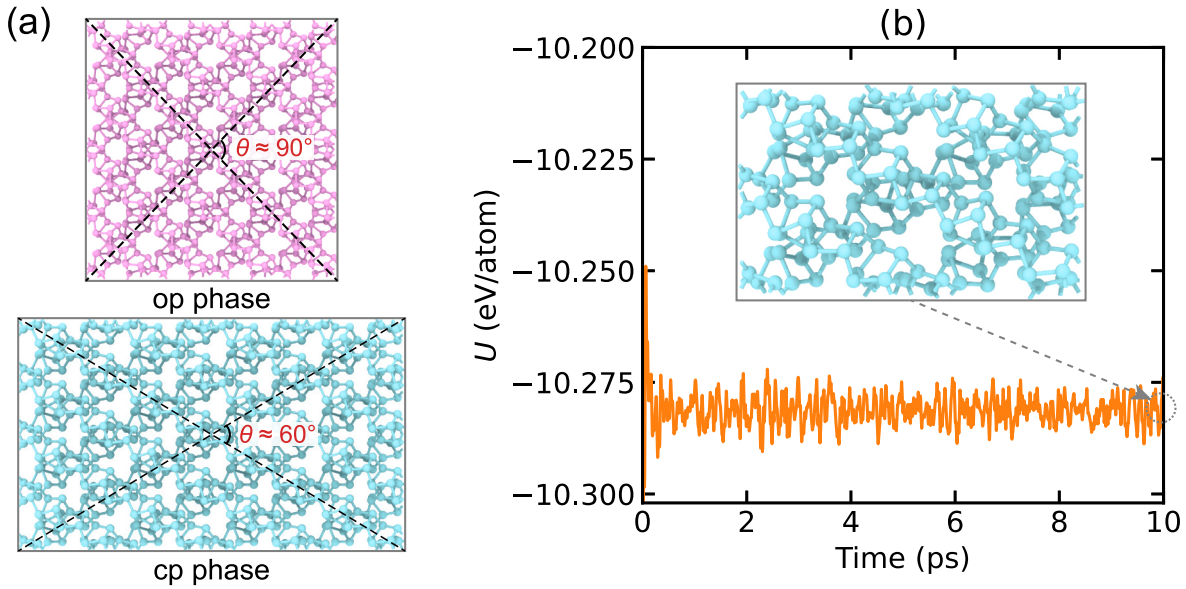

Fig. 3. (a) The atomic structure of parent op phase and transformed cp phase of monolayer VP. Here, for clarity, the 4 × 4 × 1 supercell is presented for both op and cp phases. (b) Total energy U of the 2 × 2 × 1 supercell of the cp phase of monolayer VP at 300 K calculated by AIMD simulations. The inset shows the structure of cp phase at 10 ps extracted from AIMD simulations.

Table 2
A comparison of lattice constants and mechanical properties of op and cp phases of monolayer, bilayer, and bulk VP structures. The lattice constants l_x, l_y, and l_z are crystal lengths in the x, y and z directions, respectively, which all are in unit of Å. The parameter α denotes the plane angle (from the top view) of the cross sub-nano rods as shown in Fig. 3(a), which is in unit of degree. The elastic constants C_{11}, C_{22}, C_{12}, and C_{66} are obtained by Eq. (4). E, G, and υ_{in} represent the Young's modulus, shear modulus, and in-plane Poisson's ratio, respectively. All the elastic constants and moduli are in unit of GPa.

VP	Monolayer		Bilayer		Bulk	
	op phase	cp phase	op phase	cp phase	op phase	cp phase
l_x	8.89	11.10	9.03	11.07	9.10	11.23
l_y	9.00	6.60	8.89	6.72	8.92	6.73
l_z	/	/	/	/	20.56	21.36
α	89.2	61.4	89.2	62.6	88.8	61.8
C_{11}	68.24	140.87	73.08	137.32	78.87	141.12
C_{22}	68.24	65.77	73.08	59.83	78.87	74.81
C_{12}	55.41	43.85	56.22	46.25	53.59	40.02
C_{66}	57.87	49.11	59.78	51.78	55.43	46.84
E	23.25	111.63	29.84	101.56	42.45	119.71
G	57.87	49.11	59.78	51.78	55.43	46.84
υ_{in}	0.81	0.67	0.77	0.77	0.68	0.53

rewrite the elastic constants in a new basis set and further calculate the orientation-dependent Young's modulus $E(\theta)$, shear modulus $G(\theta)$, and Poisson's ratio $\upsilon_{in}(\theta)$ of 2D rectangular system based on the following formula [32,33]:

$$\begin{aligned} E(\theta) &= 1\Big/\left(S_{11}a^4 + S_{22}b^4 + (S_{66} + 2S_{12})a^2b^2\right), \\ G(\theta) &= 1\Big/\left(4(S_{11} + S_{22} - 2S_{12})a^2b^2 + S_{66}\left(a^2 - b^2\right)^2\right)\Big), \\ \upsilon_{in}(\theta) &= -E(\theta)\left((S_{11} + S_{22} - S_{66})a^2b^2 + S_{12}\left(a^4 + b^4\right)\right), \end{aligned} \tag{5}$$

with

$$a = \cos(\theta),\ \ b = \sin(\theta), \tag{6}$$

in which θ denotes the angle between the new axis and the original $+x$ axis. S_{11}, S_{22}, and S_{66} in Eq. (5) are compliance constants that can be obtained by inverting the elastic constants matrix as defined in Eq. (4).

We calculated the elastic constants of VP structures on the basis of stress-strain relationship (Eq. (4)) with the aid of VASPKIT package [34]. Each elastic constant component was determined by using the first-order derivative of the stress-strain curve that contains nine small strains ranging from −2% to 2% in the elastic regime. For elastic tensor calculations of both op phase and cp phase, the thickness L_z of monolayer, bilayer and bulk VP structures, respectively, defined as L_z^0, $2L_z^0$ and $2L_z^0$, where L_z^0 equalling to the layer separation in the corresponding bulk VP. As listed in Table 2, L_z^0 equals to 10.28 and 10.68 for op phase and cp phase, respectively. All elastic constant components together with E, G, and υ_{in} in the original $+x$ axis are listed in Table 2, while the orientation-dependent $E(\theta)$, $G(\theta)$, and $\upsilon_{in}(\theta)$ obtained by Eq. (5) are presented in Fig. 4.

The elastic constants obtained above can be employed to examine the mechanical stability of 2D VP structures including both op and cp phases. On the basis of the Born stability criteria [35], Mazdziarz et al. [36] proposed the stability criteria for 2D rectangular lattices with the following forms:

$$\begin{aligned} &\frac{1}{2}\left(C_{11} + C_{22} + \sqrt{4C_{12}^2 - (C_{11} - C_{22})^2}\right) > 0, \\ &\frac{1}{2}\left(C_{11} + C_{22} - \sqrt{4C_{12}^2 - (C_{11} - C_{22})^2}\right) > 0, \\ &C_{66} > 0. \end{aligned} \tag{7}$$

Substituting the elastic constants listed in Table 2 to Eq. (7), we find that the stability criteria is satisfied for all VP structures, demonstrating the mechanical stability of the parent op phase and transformed cp phase for monolayer, bilayer, and bulk VP.

From the elastic constants listed in Table 2, one can clearly find that the parent op phases of all VP structures show the similar mechanical properties in both x and y directions. However, a strongly different mechanical behavior is observed in the cp phases of VP, whose C_{11} is much larger than C_{22}. This different mechanical properties observed between op and cp phases of VP structures can be easily understood by their structures before and after phase transformation as shown in Fig. 3 (a). In the op phase, VP has a symmetry structure along x and y directions, while this symmetry is broken in the cp phase. In addition, regarding each component of elastic constants of VP before and after phase transformation, the most significant difference is observed in C_{11} of op and cp phases. Taking the monolayer VP for example, C_{11} of its cp phase is 140.87 GPa, which is more than twice the value of its op

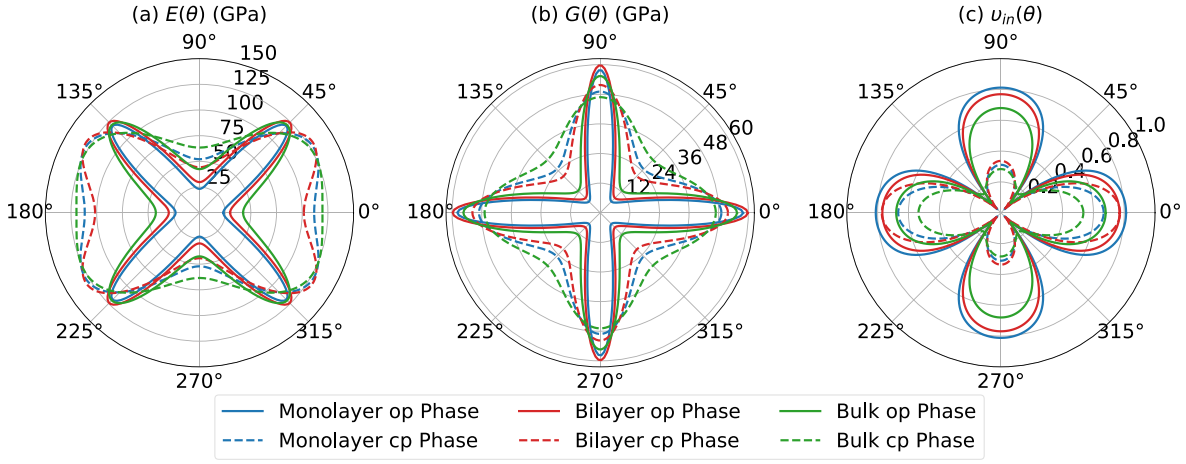

Fig. 4. Orientation-dependent (a) Young's modulus $E(\theta)$, (b) shear modulus $G(\theta)$, and (c) in-plane Poisson's ratio $\upsilon_{in}(\theta)$ of monolayer, bilayer, and bulk VP structures obtained by Eq. (5). Here, the solid line and dash line denote the results of op and cp phases for each VP structure, respectively.

counterpart (68.24 GPa). The enhancement in C_{11} induced by phase transformation further leads to a much higher E in cp phase than that in op phase. As listed in Table 2, the Young's moduli of monolayer, bilayer and bulk VP grow from 23.25, 29.84 and 42.45 GPa to 111.63, 101.56 and 119.71 GPa, respectively, after the op-to-cp phase transformation. This phase transformation-induced strengthening effect also can be observed in the $\sigma_x - \epsilon_x$ curves shown Fig. 2(a), in which the slope of $\sigma_x - \epsilon_x$ curve of cp phase at the initial tension stage is much larger than that of the op phase similarly at initial tension stage. In addition, the shear modulus of all VP structures is reduced after the phase transformation, while in this process a decrease of the in-plane Poisson's ratio is observed in monolayer and bulk VP.

From Fig. 4, it can be found that, consistent with their structures, the mechanical properties including $E(\theta)$, $G(\theta)$), and $\upsilon_{in}(\theta)$ of op and cp phases exhibit 4-fold and 2-fold rotation symmetries, respectively. Therefore, we only need to discuss the distribution of elastic properties within $0^\circ \leq \theta \leq 45^\circ$ for op phase and those within $0^\circ \leq \theta \leq 90^\circ$ for cp phase. The maximum value, minimum value, and corresponding anisotropy ratio of $E(\theta)$, $G(\theta)$, and $\upsilon_{in}(\theta)$ extracted from Fig. 4 are listed in Table 3. Here, the anisotropy ratio is defined as the ratio of the maximum value to the minimum value. From Table 3, we can see that the changes in all mechanical properties after the op-to-cp phase transformation are qualitatively similar for monolayer, bilayer, and bulk VP, though a slight quantitative difference is observed among different VP materials.

Regarding $E(\theta)$ of op phase, its maximum value $E_{\max}$ is found to locate at 45° that corresponds to the direction along sub-nano rods (see Fig. 3(a)), while its minimum value $E_{\min}$ is found at 0° that is the x axis. Specifically, $E_{\max}$ and $E_{\min}$ of op phase of monolayer VP are, respectively, 119.56 GPa and 23.25 GPa, resulting in a significant anisotropy ratio of $A_E = 5.14$. This significant anisotropy effect originates from the different deformation mechanisms of op phase of VP along these two directions. The deformation in the 45° direction is majorly attributed to the extension of bonds in the component sub-nano rods, i.e., -[P2]-[P8]-[P2]-[P9]- repeating units as shown in Fig. 1, which makes VP have the largest stiffness in this direction. The deformation along the 0° direction is mainly induced by the change of in-plane angle α as defined in Fig. 3 (a), i.e., the relative rotation between cross rods. As a result, in this direction VP will have a relatively small stiffness. The deformation mechanisms of VP will be further investigated in details in the section 3.3. Similar to its op counterpart, $E_{\max}$ of the cp phase of VP is found at the directions along the sub-nano rods, i.e., now at $\theta \sim 30^\circ$ as shown in Fig. 3(a). However, $E_{\min}$ of cp phase is found at the y direction of 90°, which is totally different to the x direction of its op counterpart. It also can be found that, A_E of the cp phase of monolayer, bilayer, and bulk VP is 2.45, 2.93, and 1.98, respectively, which is much smaller than the corresponding value of 5.14, 4.16, and 2.84 of op phase. This result demonstrates a distinct distribution of $E(\theta)$ between these two phases of VP.

Table 3
The maximum value, minimum value, and anisotropy ratio of $E(\theta)$, $G(\theta)$, and $\upsilon_{in}(\theta)$, which are extracted from Fig. 4 for op and cp phases of monolayer, bilayer, and bulk VP. The subscripts "$_{max}$" and "$_{min}$" denote the corresponding maximum value and minimum value, respectively. A_E, A_G, and A_υ denote the anisotropy ratio of $E(\theta)$, $G(\theta)$ and $\upsilon_{in}(\theta)$, respectively. All elastic moduli are in the unit of GPa, while the others are dimensionless.

VP	Monolayer		Bilayer		Bulk	
	op phase	cp phase	op phase	cp phase	op phase	cp phase
$E_{\max}$	119.56	127.95	124.23	129.86	120.70	125.64
$E_{\min}$	23.25	52.13	29.84	44.26	42.45	63.67
A_E	5.14	2.45	4.16	2.93	2.84	1.98
$G_{\max}$	57.87	49.11	59.78	51.78	55.43	46.84
$G_{\min}$	6.42	25.95	8.43	20.98	12.64	30.26
A_G	9.02	1.97	7.09	2.47	4.39	1.55
$\upsilon_{\max}$	0.81	0.67	0.77	0.77	0.68	0.53
$\upsilon_{\min}$	0.03	0.11	0.04	0.06	0.09	0.16
A_υ	24.56	5.96	19.62	13.63	7.66	3.24

The op and cp phases of VP have the similar distribution of $G(\theta)$, which has the maximum at the x or y direction and the minimum at the direction of 45°. But the anistropy of $G(\theta)$ is different for op and cp phases. Specifically, A_G of op phase is in the range of $4.39 \sim 9.02$, which is much higher than the value of its cp counterpart that ranges from 1.55 to 2.47. The significantly lower A_G of cp phase is mainly attributed to the much larger $G_{\min}$ after the op-to-cp phase transformation. For instance, $G_{\min}$ of monolayer VP within the cp phase is 25.95 GPa, which is four times larger than 6.42 GPa of its counterpart within the op phase.

We find in Fig. 4 that υ_{in} is very close to zero at 45° for both op and cp phases of VP, which is especially apparent for the op phase of monolayer and bilayer VP with $\upsilon_{\min}$ being only 0.03 and 0.04, respectively. This near-zero Poisson's ratio found in the specific in-plane direction of VP structures indicates that when VP is stretched or compressed in this direction, the length of its transverse direction can keep almost unchanged. This zero in-plane Poisson's ratio together with the aforementioned negative out-of-plane Poisson's ratio (see Fig. 2(d)) indicates that the VP structures are excellent auxetic 2D materials, which are thus expected to have widespread applications in fields such as medicine/tissue engineering and aerospace [37,38]. The maximum Poisson's ratio $\upsilon_{\max}$ of op and cp phases is found at the 0° (x axis) direction. Specifically, values of $\upsilon_{\max}$ are 0.81, 0.77, and 0.68 for the op phase of monolayer, bilayer and bulk VP structures, respectively, while the corresponding

values of their cp counterparts are 0.67, 0.77, and 0.53. These values are consistent with the results obtained from the tensile simulation as shown in Fig. 2(c). Moreover, the in-plane Poisson's ratio of op phase of VP structures is found to generally decrease with increasing thickness. This thickness dependence of Passion's ratio is attributed to the following mechanism. In bulk VP, the interaction between layers can constrain the out-of-plane deformation and further reduce the in-plane contraction along the *y* direction when it is stretched along the *x* direction, which finally leads to a relatively small υ_{in}. Due to the absence of neighboring layers, monolayer VP has more freedoms to deform in the out-of-plane direction, which results in a relatively large υ_{in}. The degree of out-of-plane constraints in bilayer VP structures is between that of their monolayer and bulk counterparts, leading to a υ_{in} between the values of monolayer and bulk VP as shown in Fig. 2(c). The similar mechanism was also demonstrated by Ref. [16] in the Bi_2O_2Se system.

3.3. Extremely large in-plane Poisson's ratio

To shed light on the structural evolution of VP structures under tension and the accompanied phase transformation as discussed above, in this section the in-plane deformation mechanism of VP structures is investigated based on the geometry analysis together with the mechanical modeling. Efforts are made to reveal the origin of extremely large in-plane Poisson's ratio found in VP structures under uniaxial tension.

Considering the unique cross structure of VP whose component sub-nano rods are linked by [P9] units (see Fig. 1), a VP cell can be approximately treated as a mechanical framework. As shown in Fig. 5 (a), in the framework model the sub-nano rods are treated as straight rods, while the [P9] unit is treated as the hinge linking two cross rods. Based on this mechanical framework model, the overall deformation of VP structures under tension is attributed to two deformation mechanisms that are, respectively, elongation and rotation of rods. Assuming the elongation and rotation angle of rods are *ds* and $d\theta$, respectively, we can obtain the following equations from the general Hooke's law

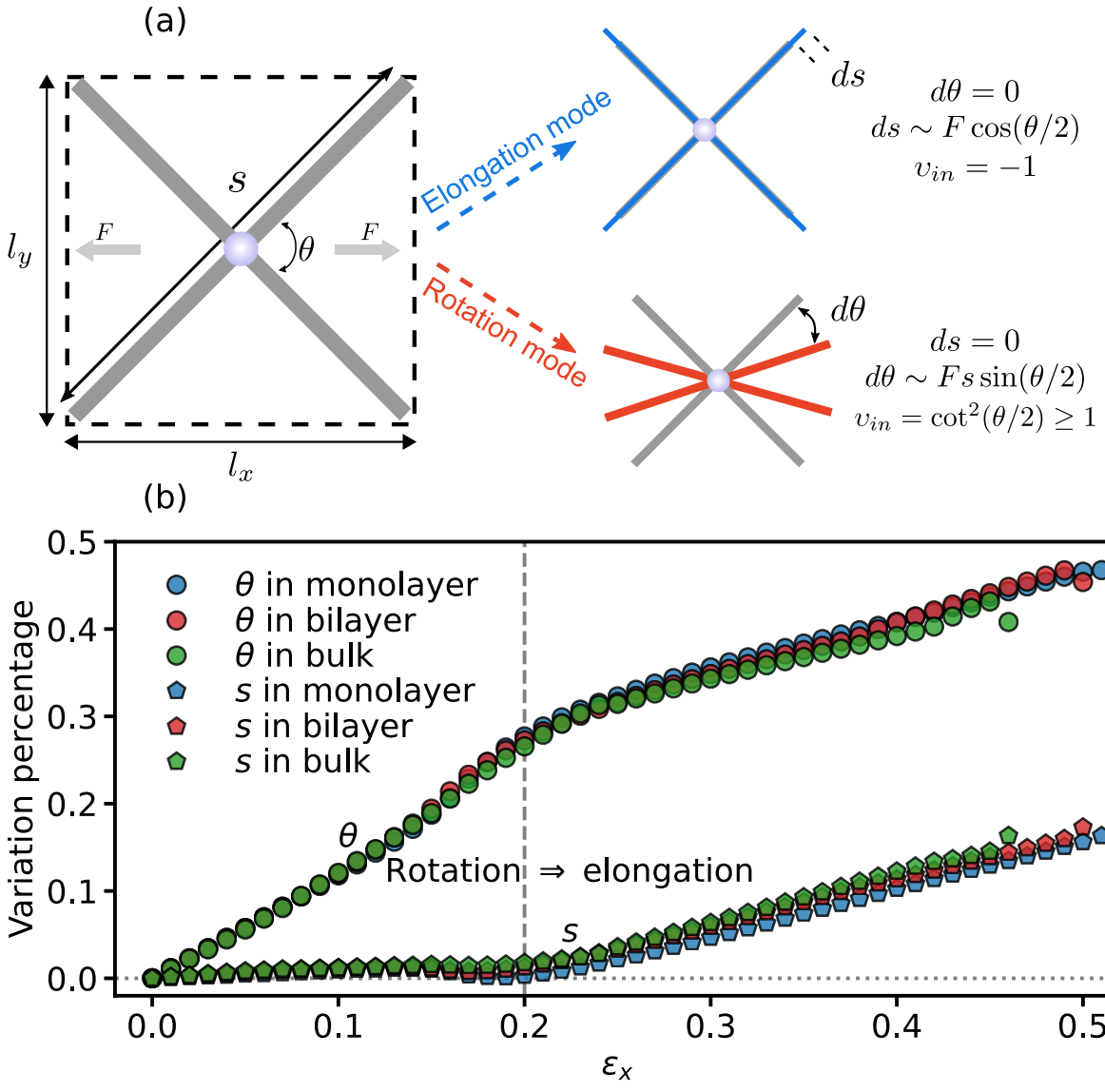

Fig. 5. (a) Illustration of the deformation mechanism of VP structures under tensile loading. Here, the tensile strain is attributed to two deformation modes including rotation and elongation. Here, *F* represents the tensile force acting on the framework, *s* represents the length of sub-nano rods along diagonal direction and θ is the in-plane angle between two cross diagonal rods. (b) The variation percentage of *s* and θ of mononlayer, bilayer, and bulk VP structures with respect to the tensile strain. The variation percentage of *S* and θ are, respectively, calculated as $\Delta s/s$ and $\Delta\theta/\theta$.

$$\begin{aligned}\frac{Fs}{2}\cos(\theta/2) &= K_s ds,\\ \frac{Fs}{2}\sin(\theta/2) &= K_r d\theta,\end{aligned} \tag{8}$$

where F is the total tensile force F acting on the framework, $\frac{Fs}{2}\cos(\theta/2)$ and $\frac{Fs}{2}\sin(\theta/2)$ are, respectively, the stretching force and rotation moment acting on the rod components, and K_s and K_r are the generalized force constants.

Meanwhile, the lengths of VP cell l_x and l_y in the x and y directions, respectively, are

$$\begin{aligned}l_x &= s\cos(\theta/2),\\ l_y &= s\sin(\theta/2).\end{aligned} \tag{9}$$

From Eq. (9) we can further have

$$\begin{aligned}dl_x &= \cos(\theta/2)ds - \frac{s}{2}\sin(\theta/2)d\theta,\\ dl_y &= ds\sin(\theta/2) + \frac{s}{2}\cos(\theta/2)d\theta.\end{aligned} \tag{10}$$

According to Eq. (2), the in-plane Poisson's ratio υ_{in} contributed by the elongation and rotation of component rods can be written as

$$\upsilon_{in} = -\frac{dl_y/l_y}{dl_x/l_x} = -\frac{ds/s + \frac{1}{2}\cot(\theta/2)d\theta}{ds/s - \frac{1}{2}\tan(\theta/2)d\theta}. \tag{11}$$

Specifically, when only considering the contribution of the elongation of rod components under the assumption of $d\theta = 0$, $\upsilon_{in} = -1$. In turn, when the contribution of elongation is excluded under the assumption of $ds = 0$, the in-plane Poisson's ratio only due to the rotation of component rods is $\upsilon_{in} = -\cot^2(\theta/2)$.

Fig. 5(b) illustrates the changes in length and rotation angle of the component sub-nano rods during the tension process of VP structures, which can be used to measure the contribution of elongation and rotation to the overall deformation of VP structures in this process. Here, the value of θ is obtained by Eq. (3), while the value of s can be directly estimated as $s = \sqrt{l_x^2 + l_y^2}$. As for all VP structures considered here, the changes in their θ and s are identical to each other. Specifically, under the initial deformation with a strain smaller than 0.2, θ increases linearly with growing strain, while s keeps almost unchanged in this process. However, when the strain grows greater than 0.2, a more significant increase is abruptly observed in s accompanied with a slower increase of θ, which makes the change in s become comparable to that in θ. This result reveals that at a strain smaller than 0.2, the deformation of VP structures is only dominated by the rotation of their component sub-nano rods. However, at a strain larger than 0.2, the elongation and rotation of sub-nano rods begin to contribute equally to the overall deformation of VP structures.

The change in the deformation mechanism observed at the strain of 0.2 can be explained as follows. In the entire tension process, θ decreases monotonically as the tensile strain increases. Meanwhile, the monotonic decrease and increase are, respectively, observed in the rotation moment $Fs \sin(\theta/2)$ and the stretching force $Fs \cos(\theta/2)$ as shown Eq. (8). Thus, at the beginning stage of the tension process with the largest θ around 45° as shown in Fig. 3(a), the rotation moment approximately equals to the stretching force. However, the deformation of VP structures under tension prefers the rotation rather than elongation of their component sub-nano rods, since the deformation is majorly governed by the deformation mode with a lower pathway energy [39]. As θ decreases with growing strain, the stretching force and the rotation moment will, respectively, increase and decrease during the tension process. Specifically, at the strain of 0.2, the impact of the increased stretching force will become comparable to that of the decreased rotation moment. This competition between two deformation modes finally results in the change in the deformation mechanism of VP structures observed in Fig. 5(b).

The deformation mechanism demonstrated here can be further adopted to explain the evolution of υ_{in} of VP structures under tension and the origin of extremely large υ_{in} observed at $\epsilon_x \approx 0.2$. When $\epsilon_x \lessapprox 0.2$, the deformation is fully dominated by rotation of the sub-nano rods. Thus, $\upsilon_{in} = -\cot^2(\theta/2)$ according to our model. Under this circumstance, υ_{in} increases from ~ 1.0 to ~ 2.46 as θ decreases from $\sim 90°$ to $\sim 65°$. This prediction is qualitatively similar to υ_{in} shown in Fig. 2(c) with different θ. However, υ_{in} obtained from DFT calculations that is in the range of ~ 0.75 to ~ 1.20 is much lower the theoretically predicted value. This quantitative difference can be understood by the fact that sub-nano rods assumed as rigid and straight rods in our mechanical model ignore the contributions of other distortions such as twist and bending in the realistic tension process; however, the twist and bending distortions can accommodate parts of the lateral deformation under uniaxial tension, which thus can dramatically reduce the magnitude of υ_{in} predicted by the mechanical model. When $\epsilon_x \gtrapprox 0.2$, in addition to the rotation, the elongation of sub-nano rods also becomes another important factor responsible for the deformation of VP structures. However, according to our model, the elongation of sub-nano rods corresponds to a constant negative υ_{in} of -1, leading to a synchronous reduction of υ_{in} as shown in see Fig. 2(c).

In addition to υ_{in}, the deformation mechanism illustrated above can be also used to reveal the evolution of three stages in $\sigma_x - \epsilon_x$ curves shown in Fig. 2(a). At $\epsilon_x \lessapprox 0.2$ where the rotation of sub-nano rods dominates the overall deformation, the stress changes gently with varied strain. But at $\epsilon_x \gtrapprox 0.2$ where the elongation of sub-nano rods starts to take part in the overall deformation, the stress becomes to sharply increase with growing strain. We attribute this difference to the fact that the bond stretching of sub-nano rods is much harder than the rotation between sub-nano rods, corresponding to a much stiffer force constant K_s compared to K_r. This also explains why Young's modulus of cp phase structures is much larger than that of their op phase counterparts (see Table 2).

Accompanied by the phase transformation, an apparent negative-stiffness stage is found in all VP structures at $0.1 \lessapprox \epsilon_x \lessapprox 0.2$. From the $U - \epsilon_x$ curves shown in Fig. 2(b), it is observed that when $0.1 \lessapprox \epsilon_x \lessapprox 0.2$, VP deforms from a configuration with the maximum U, i.e., the energy barrier and finally to a new configuration with a minimum U, corresponding to the new cp phase. The energy release during the transition process between aforementioned two deformation modes will induce a negative-stiffness behavior. To better explain the negative-stiffness behavior, in Fig. S2 (see supplementary materials) we show the change in the length of sub-nano rods s when the strain increases from 0.05 to 0.25. When $\epsilon_x < 0.1$ or $\epsilon_x > 0.2$, s is found to increase as the tensile strain grows. However, an abnormal decrease of s with increasing strain is found at the negative-stiffness stage occurring at $0.1 \lessapprox \epsilon_x \lessapprox 0.2$, which signifies the buckling of sub-nano rods during the phase transformation. In other words, the decrease of s induced by the mechanical instability during op-to-cp phase transformation results in the negative-stiffness behavior in VP structures. By virtue of their abnormal negative-stiffness behavior, the VP structures are expected to have applications as pressure sensors, artificial muscles, and actuators [40,41] in the future.

The Young's modulus E of parent phase of VP structures calculated in current work is less than 40 GPa (see Table 2), indicating an extremely flexible behavior of VP structures under uniaxial tension. Specifically, E of monolayer VP is estimated as 23.25 GPa, which is an order of magnitude lower than other monolayer 2D materials such as 1 TPa of graphene with an equivalent thickness of 3.40 Å [42], 295.57 GPa of MoS_2 with an equivalent thickness of 6.09 Å [43], and 407.62 GPa of black phosphorene with an equivalent thickness of 5.25Å [44]. As we explained above, this extremely flexible behavior of VP originates from the rotation between cross sub-nano rods without bond stretching at the initial stage of uniaxial tension process. It is noticed that, in a very recent experiment [5], E of monolayer VP measured by AFM-based nanoindentation is 1.47 TPa, which is much larger than the value (1 TPa) of

graphene that is recognized as the strongest material. Herein, we attribute this significant difference between E obtained from the present calculations and previous experiments to the strongly anisotropic mechanical response of VP structures under different loading conditions. Due to its complex cross structures demonstrated previously by Zhang et al. [5], VP shows an extremely large deformation resistance with respect to the (out-of-plane) normal loading, which may lead to the very high E measured in the nanoindentation experiments [5]. However, when under the (in-plane) uniaxial loading, the overall deformation is caused by the rotation of sub-nano rods as demonstrated above, which results in an ultrahigh flexibility property and correspondingly a very low E. Therefore, the value of 23.25 GPa calculated here and the value of 1.47 TPa obtained from the previous nanoindentation experiments actually correspond to Young's modulus of monolayer VP under in-plane tension and out-of-plane bending, respectively. The significantly different abilities of VP to resist stretching and bending deformations make VP be a stretchable but impact-resistant material, which will open the doors to the design of novel structural and functional materials in the future.

3.4. Negative out-of-plane Poisson's ratio

We have demonstrated that both bilayer and bulk VP structures have auxetic properties, i.e., negative υ_{out}, when the strain is larger than a critical value (see Fig. 2(d)). The maximum magnitude of υ_{out} ultimately can reach -0.32 for bulk VP, while the maximum value is -0.11 for bilayer VP. In this section, the underlying mechanism of auxetic properties found in VP structures is revealed based on geometry analysis together with the orbital theory.

As shown in Fig. 6(a), the overall out-of-plane deformation contains two parts including the variation of intra-layer spacing t and that of inter-layer spacing d. Specifically, it is emphasized that the atoms in individual [P9] units (as highlighted in Fig. 6) can form the covalent bonds, which result in the intra-layer spacing. These atoms can move like a hinge facilitating the rotation of two connected sub-nano rods, which thus plays a very important role in the auxetic phenomenon of bilayer and bulk VP structures.

To show the underlying mechanism of the variation of intra-layer spacing t, in Fig. 6(b) we specifically illustrate the hinge structure composed of six atoms, in which the sub-nano rods are represented by red dash lines. We find that the linked bond composed of atoms 2 and 5 (in blue) deviates from the central axis of rotation, which is represented as the purple dash line connecting midpoints of 1–3 bond and 4–6 bond (in yellow). Under this circumstance, the tension along the x axis would lead to the in-plane rotation. Specifically, atoms 1 and 3 would rotate clockwise around the central axis, while atoms 4 and 6 would rotate counterclockwise around the central axis. The in-plane rotation of these atoms is also accompanied with the movement of atoms 2 and 5 along two opposite directions, which further leads to the rotation of 2–5 bond vertically, i.e., parallel to the central axis. This rotation finally results in the increment of intra-layer spacing t (see right part of 6(b)) and thus a negative υ_{out}.

Besides the variation of intra-layer spacing t, the negative υ_{out} can be also induced by the inter-layer Pauli repulsion, i.e., the variation of inter-layer spacing d as shown in Fig. 6(c). It is found that the rotations of 2–5 bonds locating at the upper and lower layer are in opposite directions as shown by the blue arrows, which further leads to the slip of sub-nano rods near the spacing d (black arrows). Since the P atom in all VP structures has a fully filled p_z orbital, the slip phenomenon shown in Fig. 6(c) is accompanied with the large overlap of p_z orbitals, which finally results in the increment of spacing d and thus a negative υ_{out}.

Although both bilayer and bulk VP structures exhibit the negative υ_{out} under tension, as shown in Fig. 2(d), the variation of υ_{out} of bulk VP during the tension process is discontinuous at $\epsilon_x \approx 0.24$ accompanied by a step rise, which is distinct from the continuous change of υ_{out} of bilayer VP. To understand the origin of the step rise observed in the υ_{out} of bulk VP, in Fig. 7(a) we show the relative atomic displacements of bulk VP structures at different strains. From Fig. 7(a) it can be seen that the relative change between atomic displacements at ϵ_x of 0.24 and 0.23 is trivial. The similar trivial atomic displacement change is also found between the structures at ϵ_x of 0.26 and 0.25. However, an interlayer slip process accompanied with the significant relative atomic displacements is found between the structures at ϵ_x of 0.25 and 0.24. In Fig. 7(b), we further compare the average value of relative atomic displacement of monolayer, bilayer, and bulk VP during the whole tension process. It is found that the variation of atomic displacement of bilayer and monolayer VP in this process is generally smooth, while one peak locating at ϵ_x of 0.24 is observed in bulk VP, which corresponds to the interlayer slip as shown in Fig. 7(a). As for bulk VP, the interaction between layers restricts the smooth motion of interlayer atoms existing in monolayer and bilayer VP structures (see Fig. 7(b)). The resulting energy barrier in bulk VP finally leads to a maximum value of negative $\upsilon_{out} = -0.32$ before

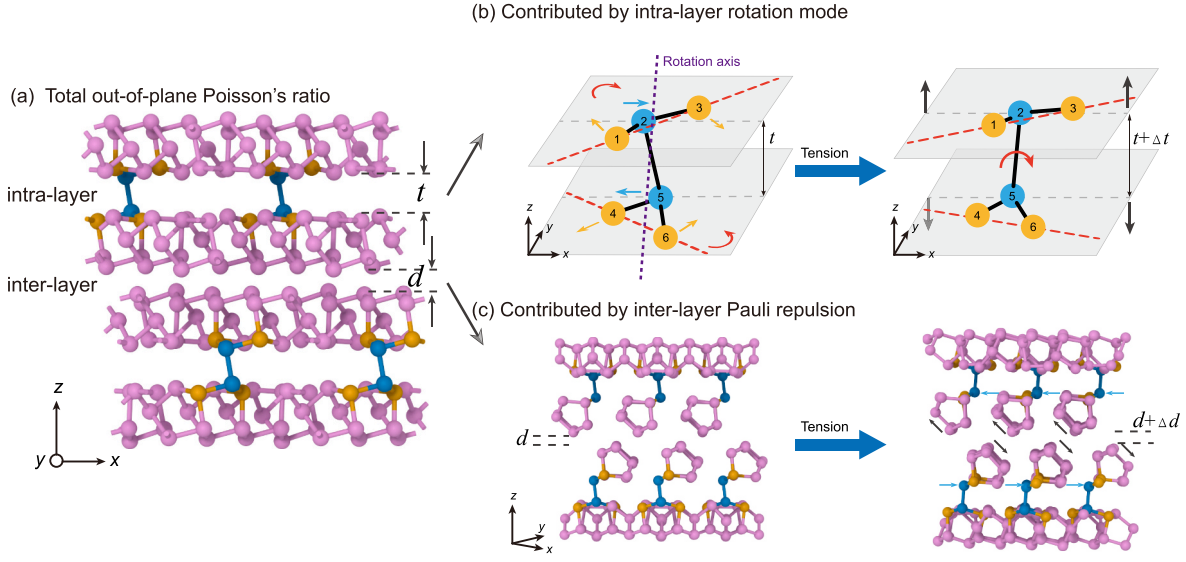

Fig. 6. (a) The illustration of the out-of-plane Poisson's ratio υ_{out} of bilayer and bulk VP structures contributed by the variation of intra-layer spacing t and inter-layer spacing d. Here, the atoms forming linked bonds through intra-layer spacing are highlighted in blue, while the atoms connecting the blue bonds and sub-nano rods are highlighted in yellow. (b, c) The illustration of intra-layer rotation and inter-layer Pauli repulsion deformation.

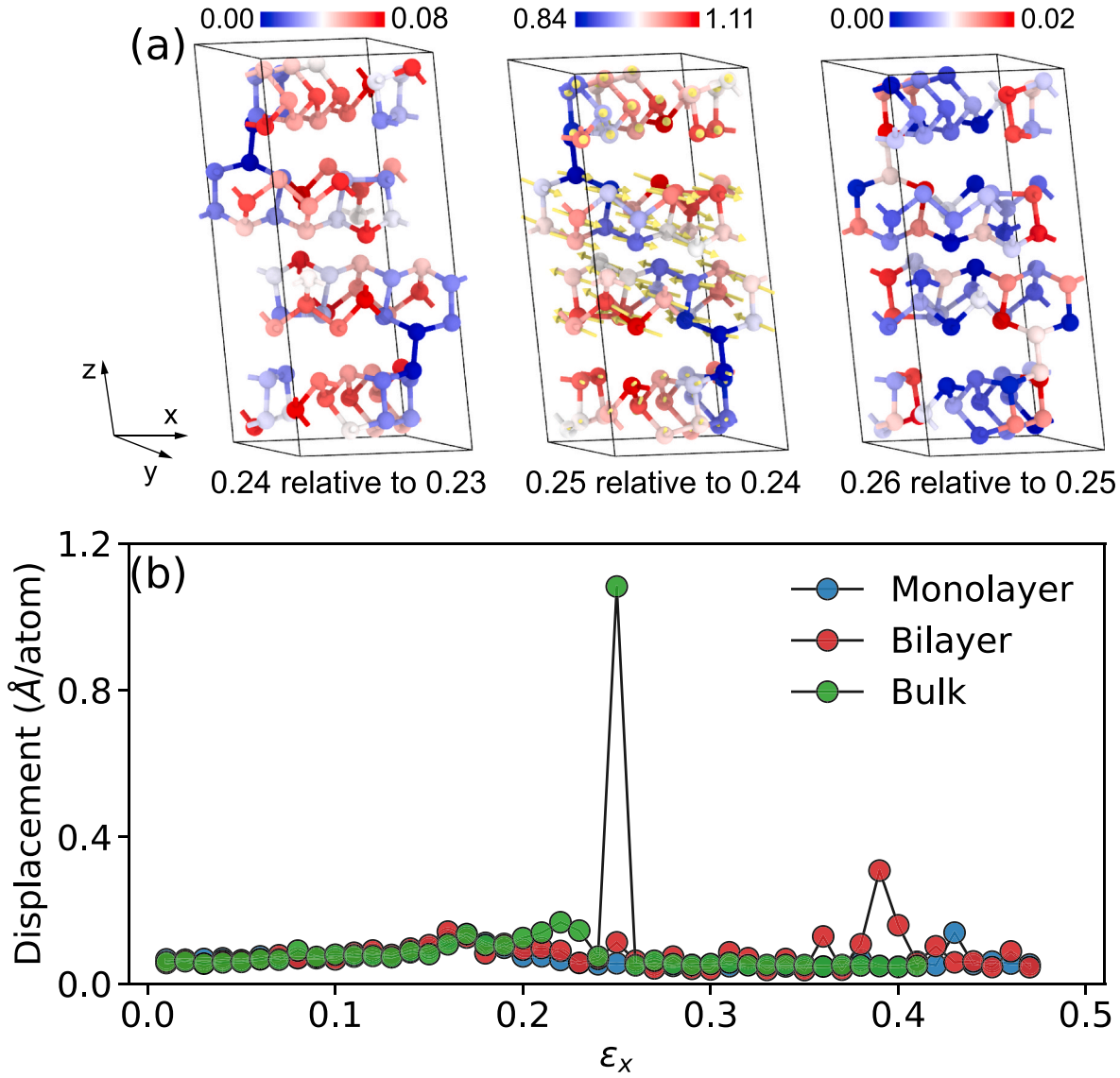

Fig. 7. (a) Relative atomic displacement of bulk VP structure at strains of 0.24 (left), 0.25 (middle), and 0.26 (right). The atoms are colored from blue to red according to their corresponding displacement magnitudes. The yellow arrows show the atomic displacement vectors. The atomic displacement is in the unit of Å. Here, the displacement vectors are not shown in the structures at strains of 0.24 and 0.26 because their magnitudes are extremely small. (b) The average value of relative atomic displacement of monolayer, bilayer, and bulk VP as a function of uniaxial tensile strain ϵ_x.

the abrupt slip process.

In order to further understand the physical source of the negative Poisson's ratio phenomenon, we calculated the energy band structures of monolayer, bilayer and bulk VP. When the strain is absent, the contribution of the p_z orbital of P atom dominates near the Fermi level (see op phase in Fig. 8(a–c)), and there is no strong interaction between the p_z orbital and other orbitals. With the increase of tensile strain, the contribution of the p_y orbital increases rapidly near the Fermi level (see cp phase in Fig. 8(a–c)). p_z and p_y orbitals show a strong hybridization. Simultaneously, VP shows a significant negative Poisson's ratio phenomenon. According to the previous study, p_z orbitals will extend to the out-of-plane direction when the VP is under the in-plane tensile strain ϵ_x. The charge density-weighted length L_z of the p_z orbital in the out-of-plane direction is $\lambda_z(\epsilon_x) = l_{p_z} f(\epsilon_x)$, where l_{p_z} is the length of the isolated p_z orbital. $\partial f(\epsilon_x)/\partial \epsilon_x > 0$ represents the influence of strain on the p_z orbital [45,46]. In addition, because VP possesses a structure much more complicated than that of other flat 2D structures such as graphene, the interaction between p_z and p_y orbitals becomes stronger when the VP is stretched along the x direction, resulting in the negative Poisson's ratio effect. This further reveals the microscopic origin of the negative Poisson's ratio in VP structures from the perspective of quantum theory, as illustrated in Fig. 6(b). Moreover, by using the tight-binding method, the interaction could be further identified to quantitatively describe the effect of the interaction between p_z and p_y orbitals on the negative Poisson's ratio [30].

In addition, we also find that when the VP possesses a negative Poisson's ratio, the conduction band and the valence band gradually overlap with each other as the strain increases, which leads to the disappearance of the band gap and thus the semiconductor-to-metal transition as shown in Fig. 8(d). The corresponding high symmetry points together with the Brillouin zones employed here are illustrated in Figs. S3–S5 (see supplementary materials). Therefore, VP is a metamaterial that possesses both negative Poisson's ratio and semiconductor-to-metal transition when under tension. The band gaps of monolayer, bilayer, bulk VP without strain are predicted to be 1.50 eV, 1.39 eV, and 1.05 eV, respectively. The critical uniaxial strain of

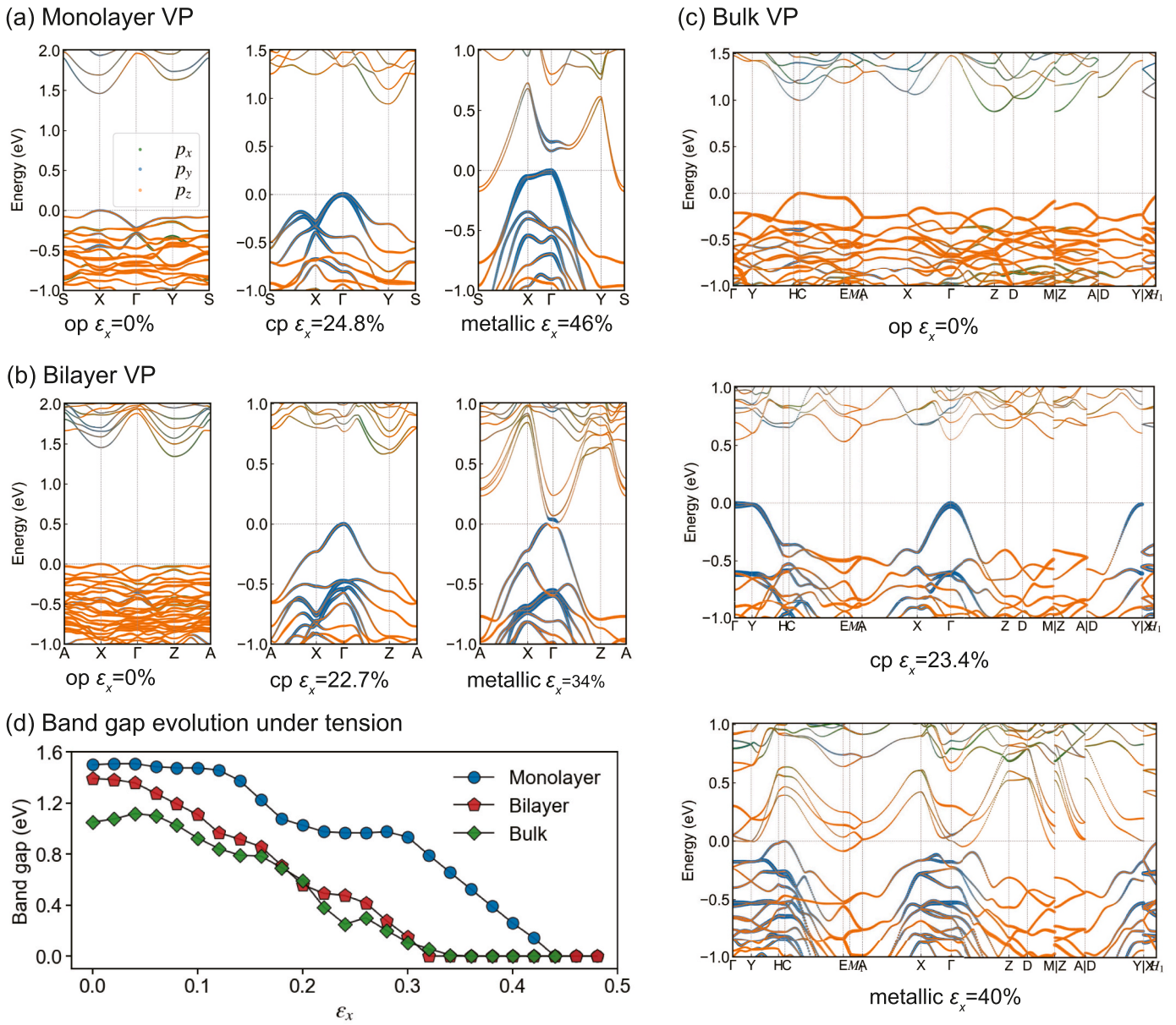

Fig. 8. Band structures of (a) monolayer, (b) bilayer and (c) bulk VP under zero strain (op phase), strain of the maximum negative υ_{out} (cp phase), and strain of semiconductor-to-metal transition (metallic phase), respectively. The green, blue, and orange lines represent the contributions of the p_x, p_y, and p_z orbitals, respectively. (d) Band gap of monolayer, bilayer, and bulk VP as a function of tensile strain ϵ_x, which indicates the semiconductor-to-metal transition.

semiconductor-to-metal transition for monolayer, bilayer, and bulk VP are 0.44, 0.32, and 0.34, respectively. The semiconductor-to-metal transition usually results in significant changes in physical properties such as resistivity, magnetism, optical reflectivity, etc [47]. These unique physical properties together with the negative Poisson's ratio makes VP have broad application prospects in the fields of piezoelectricity, information storage, sensors, field effect transistors and so on [40,48,49].

4. Conclusion

In summary, DFT calculations are performed to comprehensively investigate the mechanical responses of monolayer, bilayer and bulk VP under uniaxial tension. In addition, the mechanical properties including tensile strength, fracture strain, Young's modulus, and Poisson's ratio of VP structures are examined. Our results show a unique phase transformation from op structure to cp structure occurring in the VP, which is induced by the change of deformation mechanisms of VP during the loading process. The effect of phase transformation on the elastic properties of VP structures are investigated in details. A very strong anisotropy of elastic properties including Young's modulus, shear modulus, and Poisson's ratio are found in both op and cp phases of VP structures. Specifically, we find that both op and cp phases of all VP structures possess a zero Poisson's ratio in a specific in-plane angle. Moreover, an extremely large in-plane Poisson's ratio and a negative out-of-plane Poisson's ratio are found in the VP structures subject to certain strain. In addition, a semiconductor-to-metal transition phenomenon is observed in all VP strictures under tensile loading.

Data availability

Representative input files for DFT calculations are available online in our data repository at https://github.com/hityingph/supporting-info/. The raw data that support the findings of this study are available from

the corresponding author.

Credit author contribution statement

Penghua Ying: Conceptualization, Methodology, Software, Formal analysis, Investigation, Writing – original draft. Writing – review & editing. **Xiaowen Li**: Methodology, Software, Formal analysis, Writing – review & editing. **Xiaobin Qiang**: Software, Formal analysis. **Yao Du**: Software, Formal analysis. **Jin Zhang**: Methodology, Formal analysis, Writing – original draft, Writing – review & editing. **Lang Chen**: Supervision, Funding acquisition, Writing – review & editing. **Zheng Zhong**: Supervision, Funding acquisition, Writing – review & editing.

Declaration of competing interest

The authors declare that they have no known competing financial interests or personal relationships that could have appeared to influence the work reported in this paper.

Acknowledgments

P. Ying and J. Zhang thank Huarui Sun, Ligang Sun, and Bo Zou for helpful discussions and insightful comments. Z. Zhong acknowledges support from the National Key R&D Program of China (no. 2018YFB1502602) and the National Natural Science Foundation of China (nos. 11932005and 11772106). L. Chen acknowledges support from the National Natural Science Foundation of China (51972160) and the Science and Technology Research Items of Shenzhen (JCYJ20180504165650580).

Appendix A. Supplementary data

Supplementary data to this article can be found online at https://doi.org/10.1016/j.mtphys.2022.100755.

References

[1] A.K. Geim, Graphene: status and prospects, Science 324 (5934) (2009) 1530–1534.
[2] A. Carvalho, M. Wang, X. Zhu, A.S. Rodin, H. Su, A.H.C. Neto, Phosphorene: from theory to applications, Nat. Rev. Mater. 1 (11) (2016) 1–16.
[3] V. Tran, R. Soklaski, Y. Liang, L. Yang, Layer-controlled band gap and anisotropic excitons in few-layer black phosphorus, Phys. Rev. B 89 (23) (2014): 235319.
[4] L. Zhang, H. Huang, B. Zhang, M. Gu, D. Zhao, X. Zhao, L. Li, J. Zhou, K. Wu, Y. Cheng, et al., Structure and properties of violet phosphorus and its phosphorene exfoliation, Angew. Chem. 132 (3) (2020) 1090–1096.
[5] B. Zhang, L. Zhang, Z. Wang, Y. Li, Y. Cheng, L. Ma, J. Zhang, Cross structured two-dimensional violet phosphorene with extremely high deformation resistance, J. Mater. Chem. A 9 (2021) 13855–13860.
[6] A. Fali, M. Snure, Y. Abate, Violet phosphorus surface chemical degradation in comparison to black phosphorus, Appl. Phys. Lett. 118 (16) (2021): 163105.
[7] L. Zhang, M. Gu, L. Li, X. Zhao, C. Fu, T. Liu, X. Xu, Y. Cheng, J. Zhang, High yield synthesis of violet phosphorus crystals, Chem. Mater. 32 (17) (2020) 7363–7369.
[8] D. Akinwande, C.J. Brennan, J.S. Bunch, P. Egberts, J.R. Felts, H. Gao, R. Huang, J.-S. Kim, T. Li, Y. Li, et al., A review on mechanics and mechanical properties of 2D materials-Graphene and beyond, Extreme Mechanics Letters 13 (2017) 42–77.
[9] Z. Dai, L. Liu, Z. Zhang, Strain engineering of 2D materials: issues and opportunities at the interface, Adv. Mater. 31 (45) (2019): 1805417.
[10] J.-W. Jiang, H.S. Park, Mechanical properties of single-layer black phosphorus, J. Phys. D: Appl. Phys. 47 (38) (2014): 385304.
[11] Q. Wei, X. Peng, Superior mechanical flexibility of phosphorene and few-layer black phosphorus, Appl. Phys. Lett. 104 (25) (2014): 251915.
[12] Z.-D. Sha, Q.-X. Pei, Z. Ding, J.-W. Jiang, Y.-W. Zhang, Mechanical properties and fracture behavior of single-layer phosphorene at finite temperatures, J. Phys. D: Appl. Phys. 48 (39) (2015): 395303.
[13] Y. Lu, J. Guo, Band gap of strained graphene nanoribbons, Nano Res. 3 (3) (2010) 189–199.
[14] J. Wu, B. Wang, Y. Wei, R. Yang, M. Dresselhaus, Mechanics and mechanically tunable band gap in single-layer hexagonal boron-nitride, Mater. Res. Lett. 1 (4) (2013) 200–206.
[15] E. Scalise, M. Houssa, G. Pourtois, V. Afanas¡ev, A. Stesmans, Strain-induced semiconductor to metal transition in the two-dimensional honeycomb structure of MoS_2, Nano Res. 5 (1) (2012) 43–48.
[16] Z. Pang, T. Li, Mechanics and strain engineering of bulk and monolayer Bi2O2Se, J. Mech. Phys. Solid. 157 (2021): 104626.
[17] Lihui Zhang, Hongyang Huang, Bo Zhang, Mengyue Gu, Dan Zhao, Xuewen Zhao, Longren Li, Jun Zhou, Kai Wu, Yonghong Cheng, Jinying Zhang, Csd 1935087: Experimental Crystal Structure Determination, 2020.
[18] G. Kresse, J. Furthmüller, Efficient iterative schemes for ab initio total-energy calculations using a plane-wave basis set, Phys. Rev. B 54 (16) (1996): 11169.
[19] H. Peng, Z.-H. Yang, J.P. Perdew, J. Sun, Versatile van der Waals density functional based on a meta-generalized gradient approximation, Phys. Rev. X 6 (4) (2016): 041005.
[20] A. Stukowski, Visualization and analysis of atomistic simulation data with OVITO–the Open Visualization Tool, Model. Simulat. Mater. Sci. Eng. 18 (1) (2009): 015012.
[21] J.-W. Jiang, H.S. Park, Negative Poisson's ratio in single-layer black phosphorus, Nat. Commun. 5 (1) (2014) 1–7.
[22] X. Kong, J. Deng, L. Li, Y. Liu, X. Ding, J. Sun, J.Z. Liu, Tunable auxetic properties in group-IV monochalcogenide monolayers, Phys. Rev. B 98 (18) (2018): 184104.
[23] Y. Chen, X. Liao, X. Shi, H. Xiao, Y. Liu, X. Chen, Three-dimensional auxetic properties in group V–VI binary monolayer crystals X_3M_2 (X= S, Se; M= N, P, As), Phys. Chem. Chem. Phys. 21 (11) (2019) 5916–5924.
[24] F. Li, X. Lv, J. Gu, K. Tu, J. Gong, P. Jin, Z. Chen, Semiconducting SN_2 monolayer with three-dimensional auxetic properties: a global minimum with tetracoordinated sulfurs, Nanoscale 12 (1) (2020) 85–92.
[25] R. Peng, Y. Ma, Q. Wu, B. Huang, Y. Dai, Two-dimensional materials with intrinsic auxeticity: progress and perspectives, Nanoscale 11 (24) (2019) 11413–11428.
[26] J. Han, J. Xie, Z. Zhang, D. Yang, M. Si, D. Xue, Negative Poisson's ratios in few-layer orthorhombic arsenic: first-principles calculations, Appl. Phys. Express 8 (4) (2015): 041801.
[27] H. Wang, X. Li, J. Sun, Z. Liu, J. Yang, BP_5 monolayer with multiferroicity and negative Poisson's ratio: a prediction by global optimization method, 2D Mater. 4 (4) (2017): 045020.
[28] P. Lv, G. Tang, C. Yang, J. Deng, Y. Liu, X. Wang, X. Wang, J. Hong, Half-metallicity in two-dimensional Co_2Se_3 monolayer with superior mechanical flexibility, 2D Mater. 5 (4) (2018): 045026.
[29] X. Li, C. Huang, S. Hu, B. Deng, Z. Chen, W. Han, L. Chen, Negative and near-zero Poisson's ratios in 2D graphene/MoS_2 and graphene/h-BN heterostructures, J. Mater. Chem. C 8 (12) (2020) 4021–4029.
[30] X. Li, X. Qiang, Z. Gong, Y. Zhang, P. Gong, L. Chen, Tunable negative Poisson's ratio in van der Waals superlattice, Research 2021 (2021): 1904839.
[31] W. Voigt, Lehrbuch der Kristallphysik, Teubner Verlag, Leipzig., 1928.
[32] C. Jasiukiewicz, T. Paszkiewicz, S. Wolski, Auxetic properties and anisotropy of elastic material constants of 2D crystalline media, Phys. Status Solidi 245 (3) (2008) 562–569.
[33] C. Jasiukiewicz, T. Paszkiewicz, S. Wolski, Auxetic properties and anisotropy of elastic material constants of 2D crystalline media, Phys. Status Solidi 247 (5) (2010) 1247 [Phys. Status Solidi B 245, No. 3, 562–569 (2008)] 1247.
[34] V. Wang, N. Xu, J.-C. Liu, G. Tang, W.-T. Geng, VASPKIT: a user-friendly interface facilitating high-throughput computing and analysis using VASP code, Comput. Phys. Commun. (2021): 108033.
[35] M. Born, On the stability of crystal lattices. I, in: Mathematical Proceedings of the Cambridge Philosophical Society, vol. 36, Cambridge University Press, 1940, pp. 160–172.
[36] M. Maździarz, Comment on 'The Computational 2D Materials Database: high-throughput modeling and discovery of atomically thin crystals, 2D Mater. 6 (4) (2019): 048001.
[37] L. Rothenburg, A. Berlin, R.J. Bathurst, et al., Microstructure of isotropic materials with negative Poisson's ratio, Nature 354 (6353) (1991) 470–472.
[38] K.E. Evans, A. Alderson, Auxetic materials: functional materials and structures from lateral thinking, Adv. Mater. 12 (9) (2000) 617–628.
[39] J.-W. Jiang, T. Chang, X. Guo, H.S. Park, Intrinsic negative Poisson's ratio for single-layer graphene, Nano Lett. 16 (8) (2016) 5286–5290.
[40] R.H. Baughman, S. Stafstrom, C. Cui, S.O. Dantas, Materials with negative compressibilities in one or more dimensions, Science 279 (5356) (1998) 1522–1524.
[41] A.E. Aliev, J. Oh, M.E. Kozlov, A.A. Kuznetsov, S. Fang, A.F. Fonseca, R. Ovalle, M. D. Lima, M.H. Haque, Y.N. Gartstein, et al., Giant-stroke, superelastic carbon nanotube aerogel muscles, Science 323 (5921) (2009) 1575–1578.
[42] C. Lee, X. Wei, J.W. Kysar, J. Hone, Measurement of the elastic properties and intrinsic strength of monolayer graphene, Science 321 (5887) (2008) 385–388.
[43] S. Bertolazzi, J. Brivio, A. Kis, Stretching and breaking of ultrathin MoS_2, ACS Nano 5 (12) (2011) 9703–9709.
[44] B. Zhang, L. Zhang, N. Yang, X. Zhao, C. Chen, Y. Cheng, I. Rasheed, L. Ma, J. Zhang, 2D Young's modulus of black phosphorene with different layers, J. Phys. Chem. C 126 (2) (2022) 1094–1098.
[45] G. Qin, Z. Qin, Negative Poisson's ratio in two-dimensional honeycomb structures, npj Computational Materials 6 (1) (2020) 1–6.
[46] S. Woo, H.C. Park, Y.-W. Son, Poisson's ratio in layered two-dimensional crystals, Phys. Rev. B 93 (7) (2016): 075420.
[47] S.Y. Kim, M.-C. Lee, G. Han, M. Kratochvilova, S. Yun, S.J. Moon, C. Sohn, J.-G. Park, C. Kim, T.W. Noh, Spectroscopic studies on the metal–insulator transition mechanism in correlated materials, Adv. Mater. 30 (42) (2018): 1704777.
[48] S. Mao, J. Chang, H. Pu, G. Lu, Q. He, H. Zhang, J. Chen, Two-dimensional nanomaterial-based field-effect transistors for chemical and biological sensing, Chem. Soc. Rev. 46 (22) (2017) 6872–6904.
[49] X. Tang, L. Kou, Two-dimensional ferroics and multiferroics: platforms for new physics and applications, J. Phys. Chem. Lett. 10 (21) (2019) 6634–6649.